COMPUTATIONAL AERODYNAMIC PERFORMANCE OF MIXED-FLOW TURBINE BLADE DESIGN

Zine Khelloufi Omar* **– Hamel Mohammed – Hamidou Mohamed Kamel**

Laboratory of Applied Mechanics, Faculty of Mechanical Engineering, University of Science and Technology of Oran - Mohamed-Boudiaf BP 1505, El M'Naouer,31000, Oran, Algeria

ARTICLE INFO

***Article history*:**
Received: 8.3.2016.
Received in revised form: 21.5.2016.
Accepted: 1.6.2016.

Keywords:
Mixed flow turbine
Turbocharger
Blade angle
Incidence angle
CFX

Abstract:

The performance of two mixed flow turbocharger turbine rotors is numerically investigated. Significantly, the two rotors differ mainly in their inlet angle geometry, one has a constant blade angle (rotor A) and the other has a nominal constant incidence angle (rotor B). Since experimental data alone are not sufficient for understanding the detailed flow field within the turbocharger turbine stage, a complete 3-D Computational Fluid Dynamics model is developed using commercial software Ansys CFX. The model is validated against experimental data for all steady conditions. This study presents a numerical performance prediction of two mixed flow turbine rotors for a wide range of rotational speeds and pressure ratios. The influence of inlet blade angle on the turbine performances is also investigated.

1 Introduction

Recent turbochargers for medium and large size diesel or gas engines are forced to undergo higher pressure ratios and higher turbocharger efficiencies which lead to highly loaded turbine design. One main reason for higher pressure ratios is the application of the so-called Miller principle with early inlet valve closing to comply with future exhaust regulation whose process requires higher boost pressure than conventional working pressure. Simultaneously, increasing power density of the turbocharger demands higher flow capacity for a compact design. Therefore, turbine design specifications usually stand out of conventional area of radial inflow turbines. Such particular design requirements inherently ask high specific speed designs with associated efficiency drop partly due to higher exhaust kinetic energy losses. High specific speed design produces a rotor with large radius ratio of rotor exit to inlet for large exducer area where the choice of overall geometry design option is heavily limited. Secondary flow effects are not easily controlled, and at rotor exit more complicated non-uniform flow field is established. To achieve higher loading and higher flow in effective ways, a positive inlet blade angle can be applied to radial-inflow rotor design, but it is not common due to increased bending stresses of the rotor. Another feasible option is the mixed-flow rotor with radial sections of the blade retained, which is now popular in most highly loaded and high specific speed turbocharger turbines.

The mixed flow turbines combine the advantages of both the axial and radial inflow turbine. They can be fitted with a ring of guide vanes or nozzles depending on the type of flow, steady or pulsating, on the size of the machines and its compactness. They are available with single or twin entry scroll for damping the out of phase of the working fluid flow. Their peak efficiency is reduced, shifted towards a lower

* Corresponding author.
E-mail address:omar_zine_gm@yahoo.fr .

dimensionless ratio U/C (the rotor mean peripheral velocity / isentropic expansion absolute velocity), but presents optimal operations over a wide range of applications when compared to the radial inflow turbines. Three mixed flow turbine rotors, named A, B and C were designed and tested at Imperial College by [1] and [2]. The first one presents 12 blades and is designed with a camber line keeping the inlet blade angle fixed at 20°along the leading edge. The second one possesses the same number of blades but with a different camber line giving a nominally constant incidence angle, and a shorter axial length. Its blade angle at the mean inlet radius is kept at 20°. The third one is identical to the rotor A with a reduced blade number to 10 instead of 12. The turbine was designed to match the design conditions presented in Table 1 and tested by several researchers for steady and unsteady flow performance analysis, [3] developed an optimization procedure for the preliminary design of radial and mixed turbine. [4] studied the effect of the geometry of the volute on the performance of mixed flow turbines; they took two volutes and two different rotors. [5] carried a survey on the flow conditions of discharge from the exhaust pipe of two mixed turbines. [6, 7] measured steady and unsteady flow performance in a mixed turbocharger turbine flow. [8] measured the unsteady performances of mixed flow turbine, using laser Doppler velocimetry LDV technique. [9] designed a new nozzle vane ring to match the 3-dimensional features of the mixed-flow rotor leading edge, have tested the VG mixed-flow turbine performance at different vane angle settings, under steady and unsteady conditions. [10] performed a numerical study in aerodynamic function of the mixed flow turbine in a turbocharger; velocity of the cross sections was evaluated, and secondary flow structure analyzed. [11] contributed to the understanding of the differences between turbine configurations and assessed performance of the mixed flow turbine across the two main groups, single and twin-entry. [12] carried four major extensive pulsating flow CFD simulations, and investigated the effects of flow frequency and speed on a performance of the mixed flow turbine, they have conducted the simulations at 50% and 80 % design speed for both 20 Hz and 80Hz pulsating flow inlet conditions. The use of CFD is becoming widespread due to advances in the development of numerical methods and an increase in achievable computational power. [13] used ANSYS-CFX to perform a numerical performance prediction of a mixed flow turbine, and also investigated the influence of the space between the tip of the rotor blades and the casing. [14] studied the aerodynamic effects of waving bumps inspired by a humpback whale fin on the leading edge of a turbine blade.

This study presents a numerical performance prediction of the two mixed flow turbines keeping the same volute, but with different rotor type named A and B for a wide range of rotational speeds and pressure ratios. The obtained results are compared with the experimental data of [1] and [2]. The influence of the two rotors geometry on the performances will also be investigated. The computational domain is created by using ANSYS ICEM CFD software and the ANSYS CFX code is used to perform the numerical solution of the compressible, steady and turbulent flow in the mixed flow turbine.

Table 1. Design conditions

Rotational speed	98000 rpm
Mass flow rate	0.414 kg/s
Total inlet temperature	923 K
Optimum velocity ration	0.61

2 Flow simulation in a mixed flow turbine

The present numerical study focuses on a blade shaped with constant rotor blade angle and with a rotor nominal constant incidence angle. Common geometric details of both rotors are given in Table 2 and the blade shapes are presented in Fig.1.

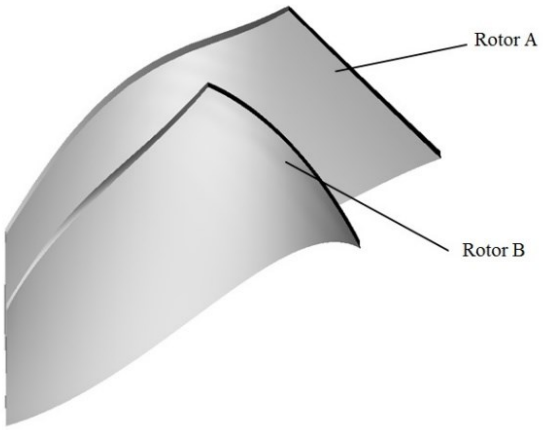

Figure 1. Geometries of the mixed flow turbine rotors.

The finite volume method implemented in the Computational Fluid Dynamics package Ansys CFX was utilized for the current study. The steady and turbulent compressible flow, Newtonian and ideal

gas through the turbine is governed by the Reynolds-Averaged Navier-Stokes Equations.

Table 2. Major dimensions of mixed-flow rotors

Rotor	**A**	**B**
Blade number	12	12
Blade inlet angle $\beta_{2,b}$	20°	Varied
Blade inlet cone angle	40°	40°
Blade exit angle $\beta_{3,b}$	-52°	-52°
Tip radius at shroud $r_{2,s}$	47.6mm	47.6mm
Tip radius at hub $r_{2,h}$	36.0mm	36.0mm
Exit radius at shroud $r_{3,s}$	39.3mm	39.3mm
Exit radius at hub $r_{3,h}$	13.5mm	13.5mm
Rotor length	40.0mm	32.5mm

The Reynolds-Averaged Navier-Stokes Equations can be expressed as follows:

Mass conservation equation:

$$\frac{\partial \rho}{\partial \mathrm{t}} + \nabla.(\rho U) = 0 \tag{1}$$

where ρ and U are density and the mean velocity vector, respectively.
Momentum conservation equation:

$$\frac{\partial(\rho U)}{\partial t} + \nabla.(\rho U * U) = \\ = \nabla\left(-p\delta + \tau - \overline{\rho u * u}\right) + S_M \tag{2}$$

where u, p, δ, τ, $\overline{\rho u * u}$ and S_M are the fluctuating velocity vector, the pressure, the Kronecker delta function, the molecular stress tensor, the Reynolds stress tensor and a source term, respectively. The Coriolis and centrifugal forces are included in the source term.

Energy conservation equation:

$$\frac{\partial(\rho H)}{\partial \mathrm{t}} + \nabla.(\rho U H - \rho\overline{uh} - \lambda \nabla T) = \frac{\partial p}{\partial t} \tag{3}$$

In this equation, H is the mean total enthalpy given by

$$H = h + \frac{1}{2}U^2 + k \tag{4}$$

where h is the mean static enthalpy, λ is the thermal conductivity, T is the mean static temperature and p is the static pressure. The additional term k in the total energy equation is the turbulent kinetic energy defined as follows:

$$k = \frac{1}{2}u^2 \tag{5}$$

Static temperature T, static pressure p and density ρ are related by the equation of state:

$$p = \rho R T \tag{6}$$

where R is the gas constant. The turbulence is modeled by the two k-ε equations which is based on the concept of turbulent viscosity. This assumes that the turbulent Reynolds stress $-\rho\overline{u_i u_j}$ can be expressed in terms of average velocity gradients and the eddy viscosity μ_t, in some way by analogy to the viscous stress τ_{ij} for Newtonian laminar flows.

$$\tau_{ij} = \mu\left(\frac{\partial U_j}{\partial x_i} + \frac{\partial U_i}{\partial x_j}\right) - \frac{2}{3}\mu\delta_{ij}\frac{\partial U_k}{\partial x_k} \tag{7}$$

$$-\rho\overline{u_i u_j} = \mu_t\left(\frac{\partial U_j}{\partial x_i} + \frac{\partial U_i}{\partial x_j}\right) - \\ -\frac{2}{3}\mu_t\delta_{ij}\frac{\partial U_k}{\partial x_k} - \frac{2}{3}\delta_{ij}\rho_k \tag{8}$$

This model assumes that the eddy viscosity μ_t is linked to the turbulent kinetic energy k and its dissipation rate ε through the following relation:

$$\mu_t = \rho C_\mu \frac{k^2}{\varepsilon} \tag{9}$$

where C_μ=0.09 and k and ε are defined through the following two equations:

$$\frac{\partial(\rho k)}{\partial t} + \nabla \bullet (\rho U K) = \\ = \nabla \bullet \left[\left(\mu + \frac{\mu_t}{\sigma_k} \right) \nabla K \right] + Pk - \rho\varepsilon \quad (10)$$

$$\frac{\partial(\rho \varepsilon)}{\partial t} + \nabla \bullet (\rho U \varepsilon) = \\ = \nabla \bullet \left[\left(\mu + \frac{\mu_t}{\sigma_\varepsilon} \right) \nabla \varepsilon \right] + \\ + \frac{\varepsilon}{K} (C_{\varepsilon 1} P_K - C_{\varepsilon 2} \rho \varepsilon) \quad (11)$$

In this model, P_k is the turbulence production and σ_k=1.00, σ_ε=1.30, $C_{1\varepsilon}$=1.44, $C_{2\varepsilon}$=1.92 are constants determined experimentally from a wide range of turbulent flows [15].

3 Numerical method

The flow solution in the mixed flow turbine is obtained by a numerical finite volume method. The ICEM CFD tool is used to build the turbine geometry and to generate the unstructured mesh.

The influence of the rotational speed on turbine performance is performed on a complete turbine stage. The turbine geometry is split into volute (stationary domain) and rotor wheel (rotating domain).

The volute and rotor domains are connected using the Generalized Grid Interface (GGI) implemented in ANSYS-CFX so that a strict conservation is maintained across the interface for all fluxes of all equations.

To analyze the coupled rotor–stator configuration, an interface between rotating and fixed components has to be defined. The Multiple Frames of Reference (MFR) allows the analysis of situations involving domains that are rotating relative to one another. For this part of the study, this feature focuses on the investigation of rotor/stator interaction for rotating machinery using the frozen rotor interface model [16]; this means that the relative position of the grids on each side of the interface does not change. In the MFR concept, a coordinate system that rotates with the turbine is used. Therefore, additional source terms including Coriolis and centrifugal forces have to be considered. Since the housing of the turbine is not rotating, the computational domain contains also regions which are described in non-rotating coordinates. Hence, the Coriolis terms and centrifugal forces are activated only in the region where rotation of the geometry occurs.

The flow domain is discretized into finite volumes of tetrahedral elements and prism elements in the near wall layer, and the y+ value is controlled between 20 and 100 in order to properly capture the high gradients inside the boundary layer by using the wall function. In order to get more detailed flow characteristics, a high mesh density is employed.

In order to analyze the quality of the mesh and see its influence on the solution, three grids have been tested with ICEM CFD. The numbers of nodes forming each of the computational grids are presented in Table 3 and Fig. 2(a), and the distributions of nodes within each domain are shown in Fig. 2(b) and Table 4.

Table 3. Number of nodes of the computational grid

	Number of nodes	
	Turbine A	Turbine B
Coarse	313 788	330 733
Medium	464 300	489 254
Fine	607 987	680 995

Table 4. Number of nodes

	Number of nodes
Turbine A	444 215
Turbine B	447 169
Volute	42 085

The pressure ratio distribution around rotor blades for the three types of computational grid is shown in Fig.3, which underlies a very thin difference in the computed pressure distribution between the three computational grid types: the coarse, the medium and the fine one. This was the main reason for adopting the medium mesh size in the rest of simulations. The computational error is fixed at 10^{-5} and the computing time was about 1 day and 7 hours for each chosen type of grid.

The integration on the finite volume equations describing the turbulent flow results in a set of discrete equations. The terms of the differential equations on the volume interfaces are obtained by a first order upwind scheme or a high resolution scheme.

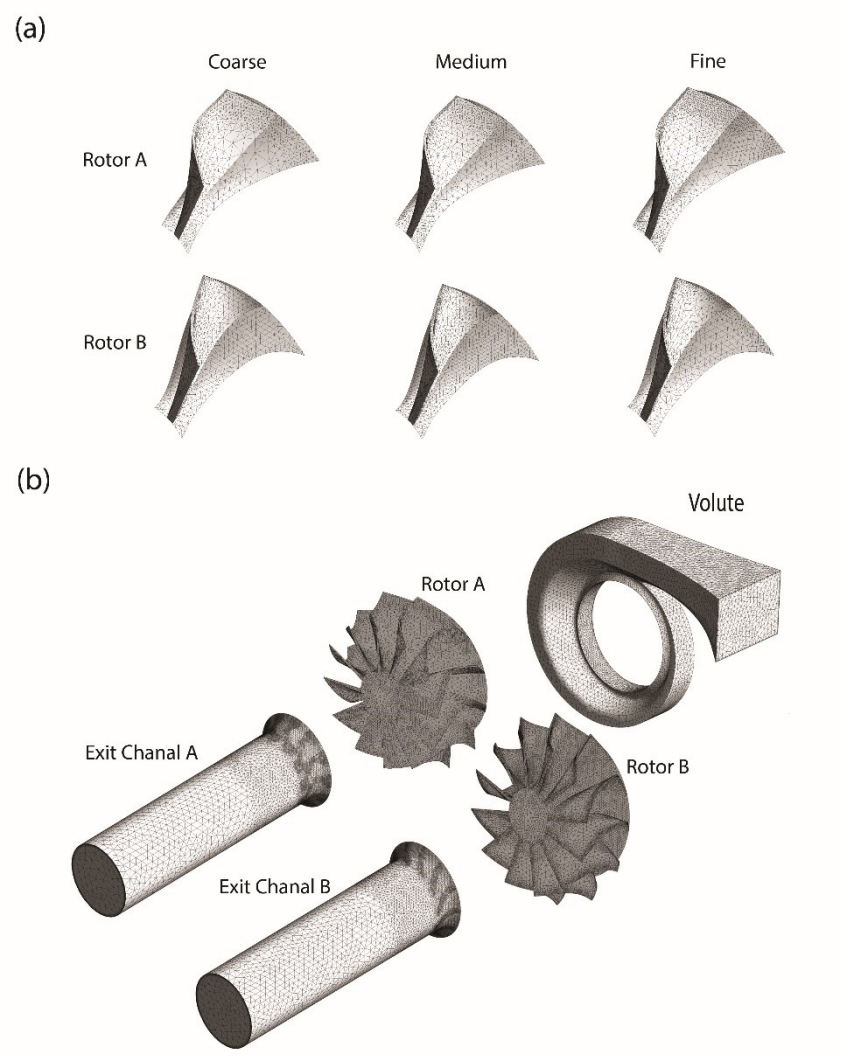

Figure 2. (a) The three computational grid types ; (b) Computational grids of the turbines.

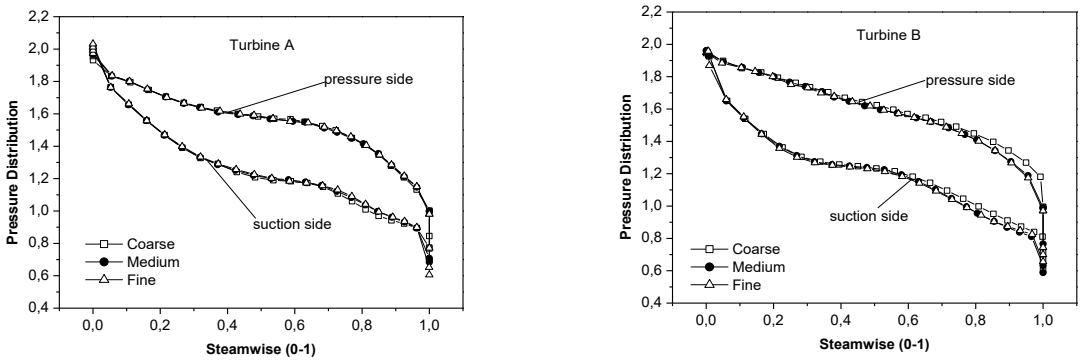

Figure 3. Pressure ratio distribution around rotor blades for three grids.

The first order upwind scheme is used to obtain an approximate solution of the flow while the high resolution scheme is used to obtain the final solution. The simulation with first order scheme is initialized using linear interpolation between boundary condition quantities and then the solution is used as an initial guess for the final simulation, which ensures a relatively rapid convergence. The pressure-

velocity coupling is achieved using a coupled solver, which solves the hydrodynamic equations (for u, v, w, p) as a single system in conjunction with a momentum-interpolation technique similar to that of [15] to prevent pressure-field oscillations as a result of the non staggered, collocated grid arrangement.
For steady state problems, the time-step behaves like an acceleration parameter, to guide the approximate solutions in a physically based manner to a steady-state solution. This reduces the number of iterations required for convergence to a steady state.
At the domain inlet, the flow is assumed subsonic, and therefore the total pressure, the total temperature and a medium intensity of turbulence (5%) in the stationary frame of reference as well as the flow direction are imposed. The turbulence quantities at the inlet boundary are obtained from the inlet hydraulic diameter and the intensity of turbulence. At the turbine outlet, where the flow is considered to be subsonic, the static pressure is imposed. On the solid boundaries, a no-slip condition is used.
At the inlet boundary of the domain shown in Fig.4, a varying total pressure and total temperature is specified for three rotational speeds corresponding to 29500 rpm, 41300 rpm and 59700 rpm respectively for 50%, 70% and 100% of the equivalent design rotational speed.

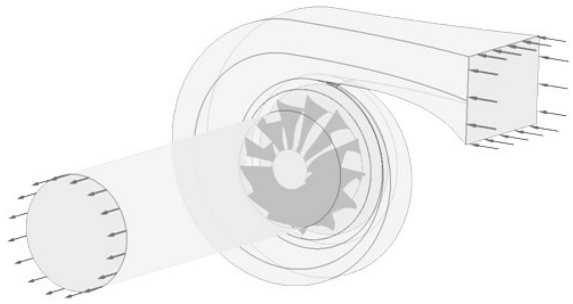

Figure 4. Mixed flow turbine.

The data boundary conditions are given in Table 5.

Table 5. Computed tests conditions

Speed	Turbine inlet total temperature	Pressure ratio
50% (29 432 rpm)	333.0 K	1.239–1.626
70% (41 266 rpm)	334.0 K	1.645–2.140
100% (59 750 rpm)	342.2 K	1.959–3.236

The data for inlet boundary condition are taken from the experimentally acquired values at the measurement plane of a cold test rig [1].
The outlet boundary condition requires the static pressure values. Therefore, constant atmospheric pressure is applied at the boundary plane.

4 Results and discussion

The numerical results are validated with experimental performance parameters in steady conditions. The steady performance of the turbine was obtained by measuring the required parameters. These are at the turbine inlet, the pressure, temperature and turbine speed. All other steady performance parameters were derived as shown in the following equations.
Pressure ratio:

$$P_r = \frac{P_{0^*}}{P_4} \tag{12}$$

Velocity ratio:

$$\frac{U_2}{C_{is}} = \frac{\omega r_2}{\sqrt{2C_P T_{0^*}\left[1-\frac{P_4}{P_{0^*}}\right]^{\frac{\gamma-1}{\gamma}}}} \tag{13}$$

Total to static efficiency:

$$\eta_{ts} = \frac{\left(h_{0^*} - h_4\right)}{C_P T_{0^*}\left[1-\frac{P_4}{P_{0^*}}\right]^{\frac{\gamma-1}{\gamma}}} \tag{14}$$

where 0 is volute inlet, 2 is rotor inlet, 4 is turbine exit and 0* is volute inlet stagnation condition.
The pressure distribution along the shroud profile has been measured for each boundary condition. The boundary conditions are given in Table 5. The results of such measurements are compared with experimental data [1] and are presented in Fig.5 and Fig.6 As far as rotor A is concerned, the expansion process is taking place across all the rotor shroud profile, at all speeds and pressure ratios. This type of pressure distribution is characteristic of accelerating flow and therefore minimal losses. Rotor B by contrast shows that the flow is over expanding and

the pressure recovery observed just upstream of the trailing edge is likely to result in flow separation especially on the suction surface. The consequence of such phenomenon is higher rotor losses.

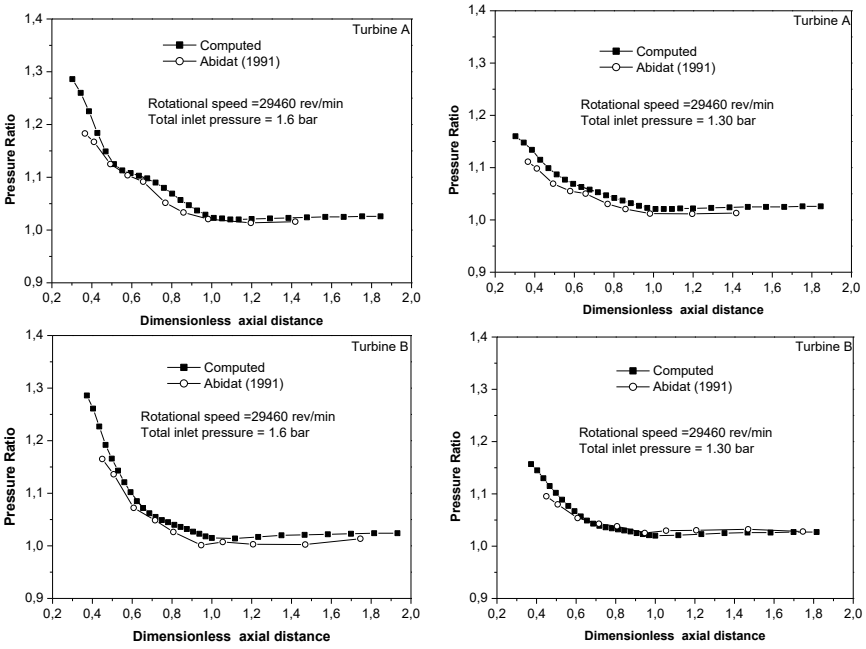

Figure 5. Mixed flow turbine shroud pressure distribution at 50% rotational speed

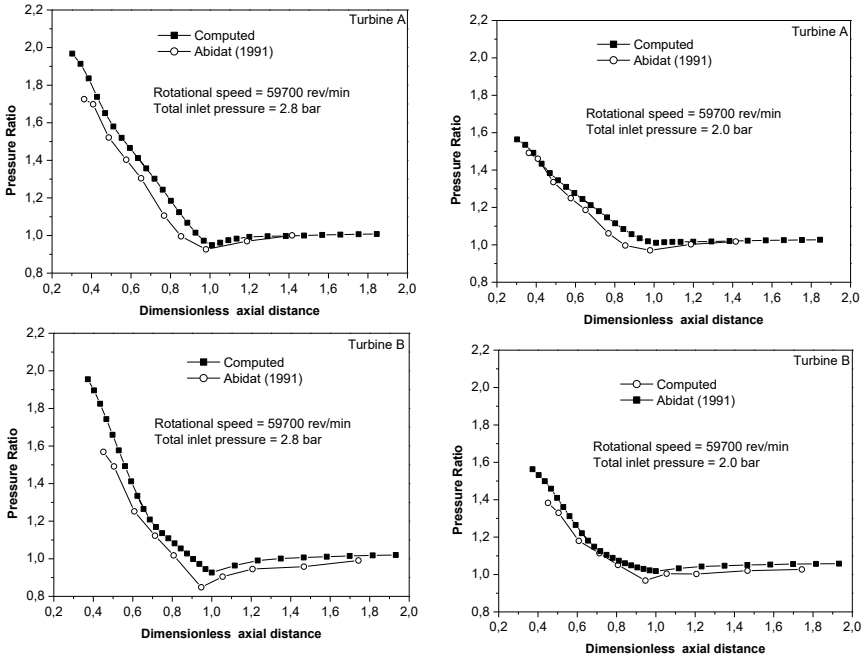

Figure 6. Mixed flow turbine shroud pressure distribution at 100% rotational speed.

Fig.7 presents total to static efficiency (η_{ts}) of the two mixed flow turbines with different type of rotor A and B for 50%, 70% and 100% of equivalent design speed versus the velocity ratio (ratio of the rotor mean peripheral velocity and the isentropic absolute velocity obtained by an expansion from the turbine inlet stagnation condition to the turbine outlet static pressure). The most striking conclusion from both experimental curves conducted on the same type of rotor, at the same laboratory is the quantitative

differences in the efficiency values, but with almost similar trends. These results do themselves explain the use of new experimental techniques.

The estimated numerical performances agree qualitatively well with the experimental ones, except for higher velocity ratio U/C, which is due to three dimensionalities of the flow path through the turbine and the formation of secondary flows mainly observed in the rotor type B. It should be pointed out that, in the CFD case, the turbine efficiency is calculated by the difference of temperatures without subtracting losses due to the seal, disk and bearing friction. The different ways of calculating the efficiency could be a significant factor of quantitative difference which is observed in our result comparison between experimental data and CFD calculations.

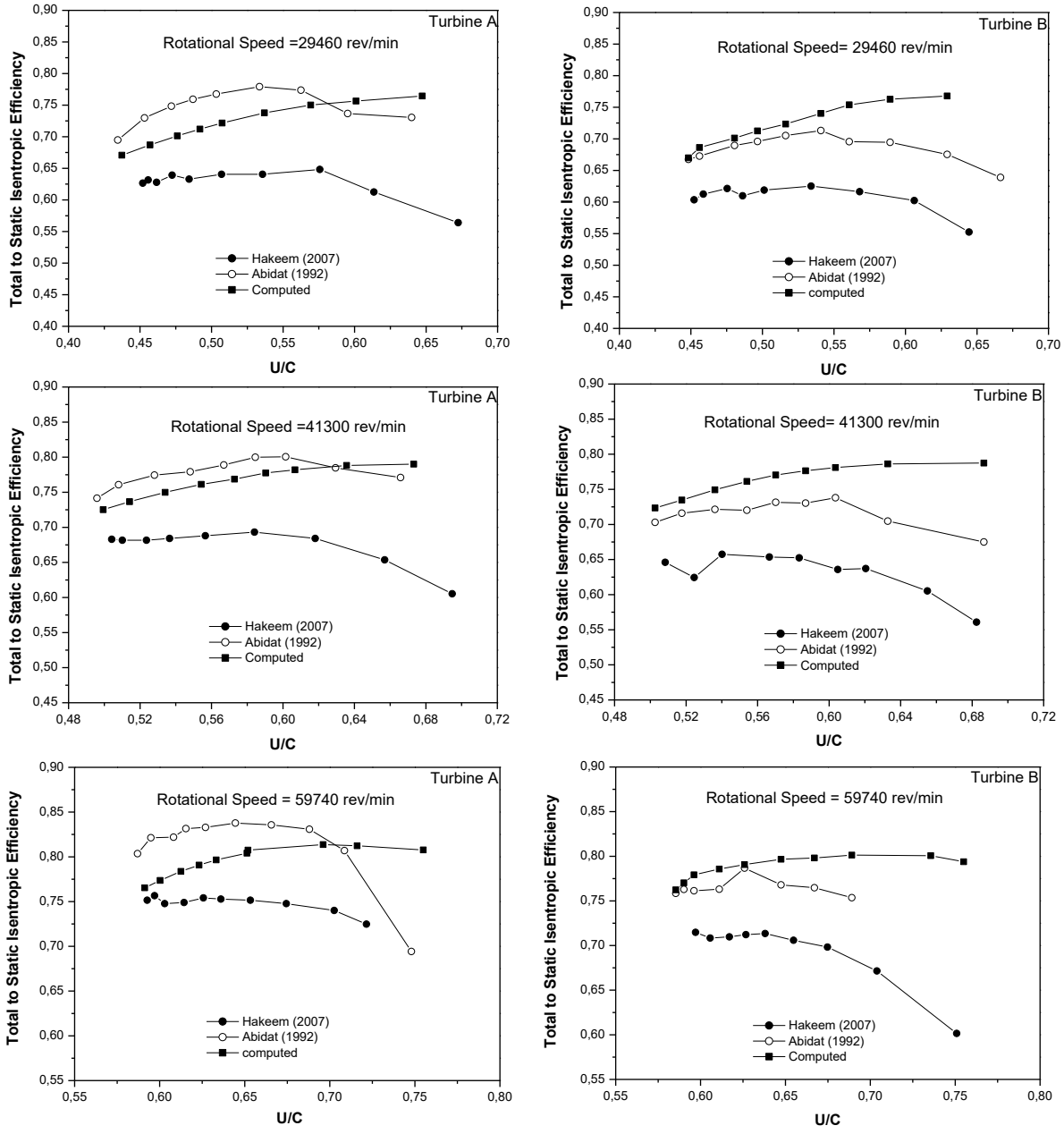

Figure 7. Mixed flow turbine total to static efficiency vs velocity ratio at 50%, 70% and 100% rotational speed.

Figure 8 presents the results of flow features in rotor inlet and outlet for a whole turbine stage at an equivalent design conditions corresponding to a total temperature $T_{0*} = 344$ K and a total pressure $P_{0*} = 2.8$ bar at the turbine inlet and a rotational speed of 59750 rpm. It shows clearly that the contours of the static pressure at two rotor A and B inlet and outlet are non periodic. The principal reason of non-periodicity is that the volute outlet flow is influenced by the tongue wake, and therefore, the flow at the rotor inlet is circumferentially non- uniform. Besides, at the outlet of the two rotors the pressure on the pressure side near the hub of the turbine B is greater than a turbine A.

Figure 9 shows the pressure ratio distribution around the rotor blade for two mixed flow turbines at 100 % rotational speed, a larger static pressure difference being between the section and pressure sides with the mixed flow turbine B especially at the entrance of the rotor.

Figure 10 and Figure 11 are prepared to capture the differences in aerodynamics inside three dimensional rotor passages of the two turbines in design conditions. Fig.10 shows the distributions of static pressure along the rotor blade suction and pressure surfaces near hub and shroud. Fig.11 shows velocity vector plotted inside the rotor passage starting from the nozzle inlet plane. In Fig.10, relatively uniform loadings are found in the rotor blades of the mixed flow turbine A, while hub loadings are strongly influenced in another rotor.

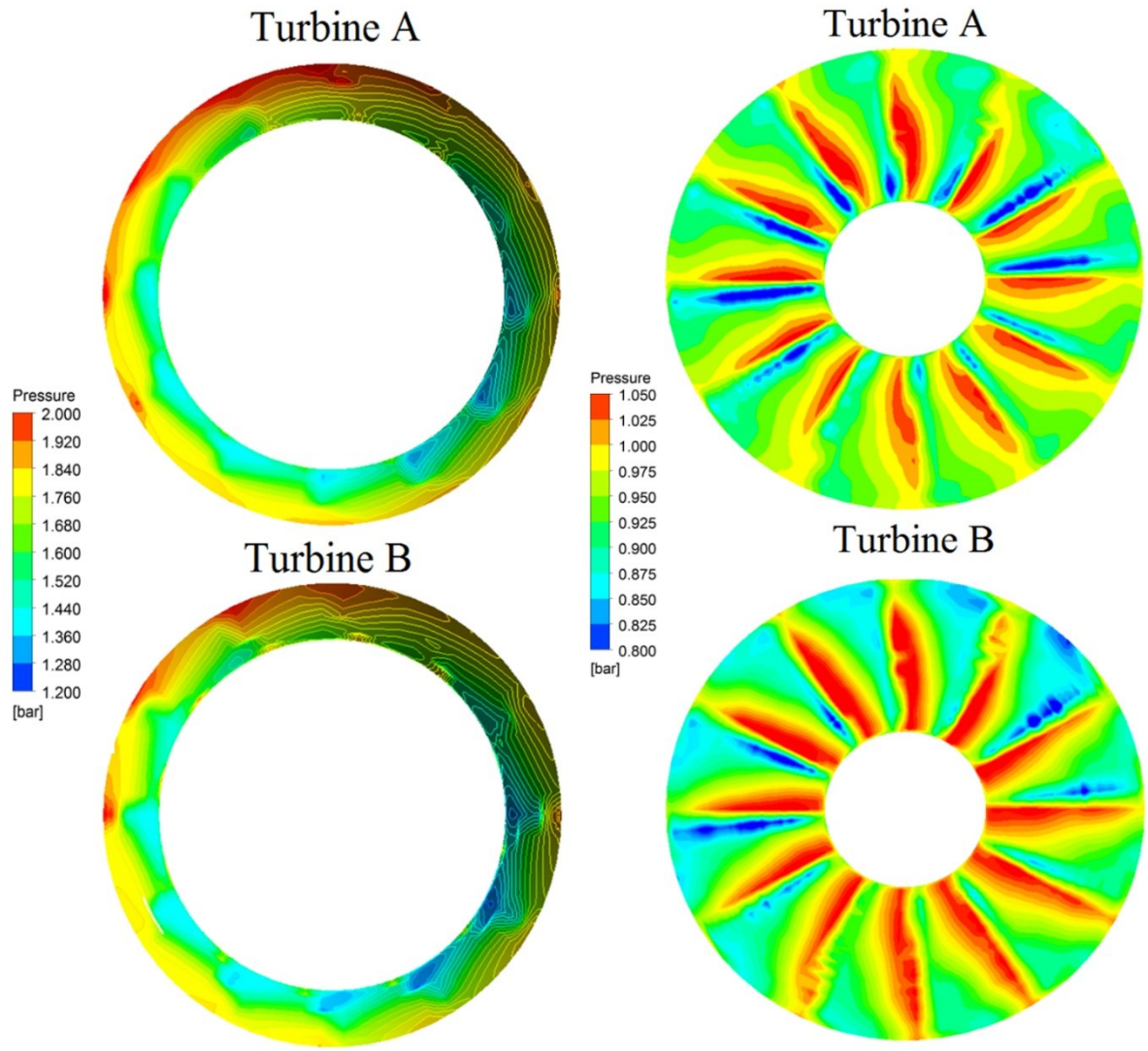

Figure 8. Rotor inlet and outlet pressure contours.

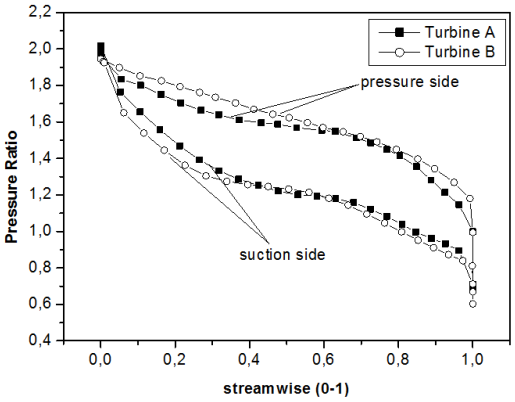

Figure 9. The pressure ratio distribution around the rotor blade for the two mixed flow turbines A and B.

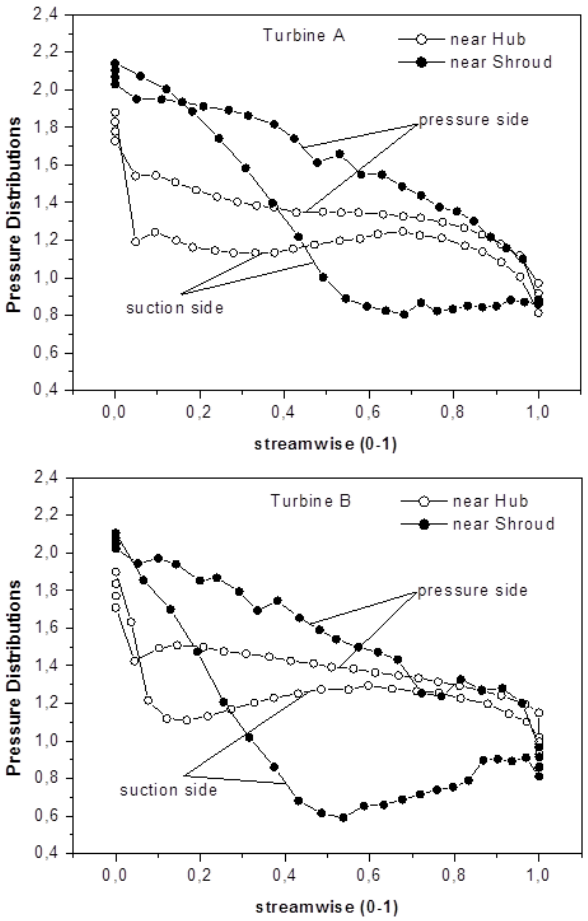

Figure 10. The pressure ratio distribution around the rotor blade for the two mixed flow turbines A and B.

The distortions of hub loading in the mixed flow turbine B are caused by a strong secondary flow developed from nozzle exit along the hub curvature, migrating from the suction surface of the rotor towards the pressure surface of the rotor, as shown in Fig.11.

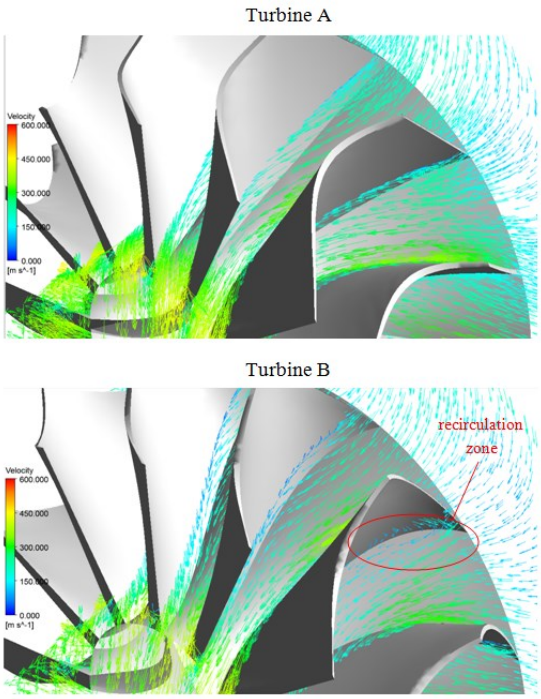

Figure 11. Velocity Vector plotted inside the rotor passage starting from the nozzle inlet plane

The secondary flow migration produces a reversed pattern of static pressure distributions along the pressure surface and the suction surface near hub. The effect of the secondary flows is decreased towards shroud due to larger radius of curvature, but another effect of tip leakage vortex becomes dominant near shroud.

Figure 12 shows the velocity angle distribution along different streamline for both turbine A and B. The difference between two rotors is clearer at the hub as the flow should follow the form of the blade.

The blade loading is illustrated in Fig.13 by the static pressure contours at one blade pressure and suction sides for the two mixed flow turbines A and B. The blade geometry generates the pressure gradient between the suction and pressure sides. As a result, the flow velocities on the suction side are higher than the velocities on the pressure side. The expansion of pressure in turbine A is larger than the turbine B so that in the suction side of the turbine B, we see a depression zone near the hub due to the inclination of the rotor.

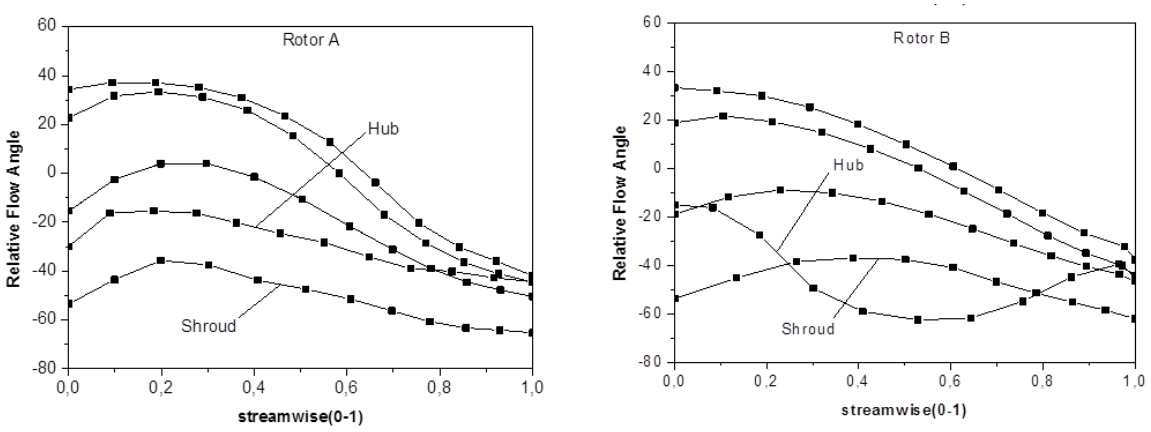

Figure 12. Velocity angle distribution along different streamline for two mixed flow turbines A and B.

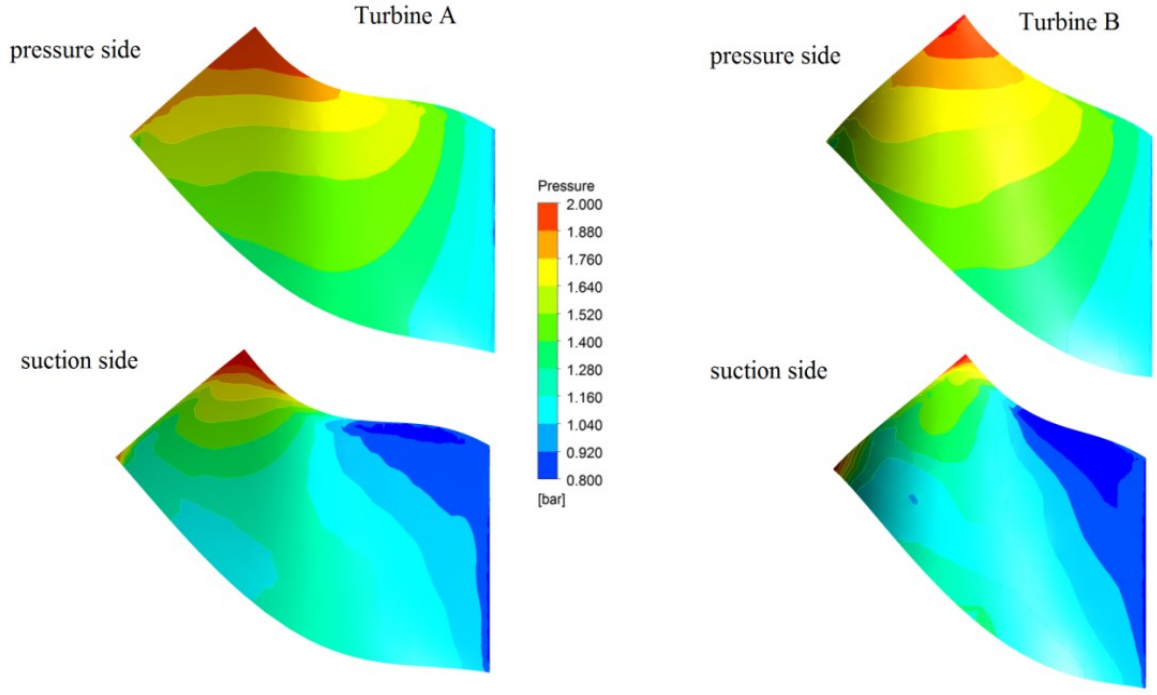

Figure 13. Mixed flow rotor blade pressure contours.

Figure 14 shows the limiting streamlines on the suction side to different azimuthal angle (0° and 180°). We see clearly that there is a recirculation zone at the suction surface for two rotors A and B. The recirculation zone in the rotor A is smaller than the rotor B, and the difference between them is made by the leading edge effect.

5 Conclusions

This paper presents a numerical performance prediction of the two mixed flow turbine rotors under inlet steady flow conditions. The ANSYS-CFX code is used to solve the highly three dimensional viscous flow. The computed pressure ratio is in reasonable agreement with experimental data.

We find that no remarkable differences are obtained from rather specialized blade shape with nominal constant incidence angle.

The efficiency characteristics of mixed flow turbines have proved to be fairly flat, providing a flat peak efficiency.

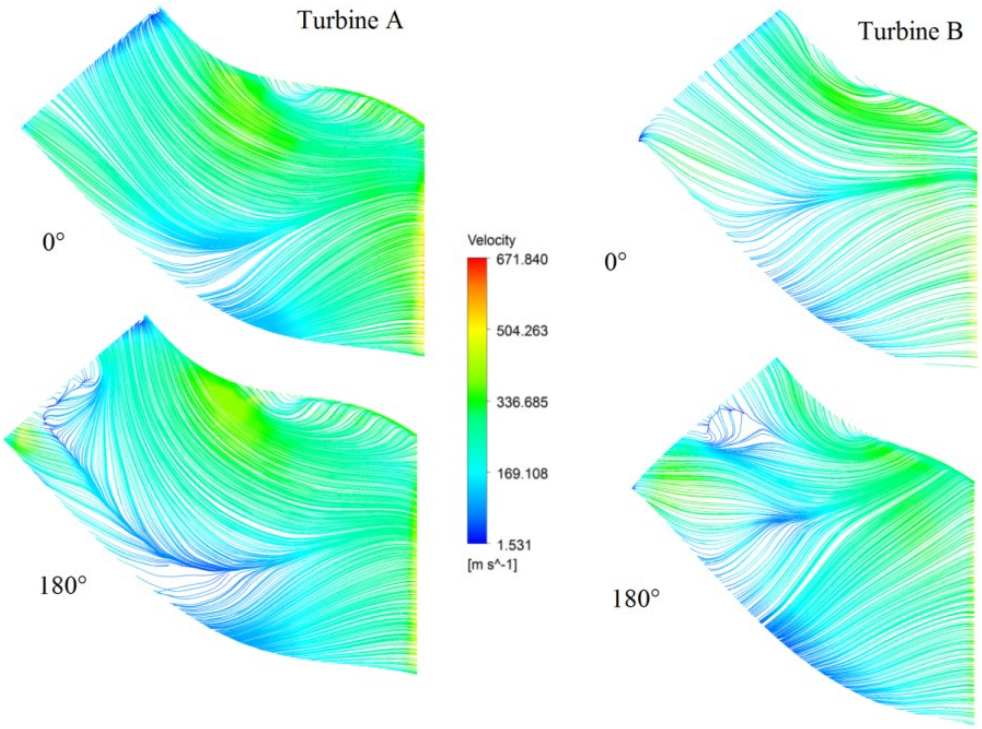

Figure 14. Limiting streamlines on the suction surface at different azimuthally angles (0° and 180°).

The benefit of the blade with forward sweep at inlet was clearly seen in shifting peak efficiency towards higher expansion ratios or lower velocity ratios. The B type rotor is capable of achieving a large pressure difference between the blade suction and pressure sides with an additional gain of transformed energy resulting in a small kinetic energy at the exit of the rotor which could reflect an appreciably benefit on the amount at the shaft work. Since the same volute is used for both rotors, we have observed a large secondary flow for the curved aerodynamic profile of rotor B leading to significant losses inferring the overall efficiency of the machine.

References

[1] Abidat, M.: *Design and Testing of a highly loaded mixed flow turbine*, University of London,1991.

[2] Abidat, M., Chen, H., Baines, H.: *Design of a highly loaded mixed flow turbine*, Arch. Proc. Inst. Mech. Eng. Part A-J. Power Energy, 21 (1992), 206, pp. 95–107.

[3] Chen, H., Baines, N. C.: *Analytical optimization design of radial and mixed flow turbines*, Arch. Proc. Inst. Mech. Eng. Part A J. Power Energy, 31 (1992), 206, pp. 177–187.

[4] Hakeem, I., Su, C.-C., Costall, A., Martinez-Botas, R. F.: *Effect of volute geometry on the steady and unsteady performance of mixed-flow turbines*, Proc. Inst. Mech. Eng. Part A-J. Power Energy, 221 (2007), 4, pp. 535–549.

[5] Chen, H., Baines, N.C.: Abidat, M.: *Exit traverse study of mixed-flow turbines with inlet incidence variation*, Proc. Instn. Mech. Engrs. 211 (1997), pp. 461–475.

[6] Karamanis, N.: *Mixed-flow turbines for automotive turbochargers : steady and unsteady performance*, Int. Jour. Eng. Res. 3 (2002), 3.

[7] Hamel, M., Abidat, M., Litim, S. A.: *Investigation of the mixed flow turbine performance under inlet pulsating flow conditions*, Comptes Rendus Mécanique, 340 (2012), 3, pp. 165–176.

[8] Arcoumanis, C., Martinez-Botas, R. F., Nouri, J. M., Su, C. C.: *Performance and Exit Flow Characteristics of Mixed-Flow Turbines*, Int. J. Rotating Mach., 3 (1997), 4, pp. 277–293.

[9] Rajoo, S., Martinez-Botas, R: *Variable Geometry Mixed Flow Turbine for Turbochargers : An Experimental Study*, Int. Jour. Fluid Mach. Sys., 1 (2008), 1, pp. 155–168.

[10] Chen, L., Zhuge, W., Zhang, Y., Zhang, S., Zhang, J.: *Investigation of the Secondary Flow Structure in the Mixed Flow Turbine for a High Pressure Ratio Turbocharger*, Vol. 6 Turbomachinery, 6 (2008), Parts A, B, C, pp. 1611–1618.

[11] Romagnoli, A., Martinez-Botas, R.: *Performance prediction of a nozzled and nozzleless mixed-flow turbine in steady conditions*, Int. J. Mech. Sci., 53 (2011), 8, pp. 557–574.

[12] Padzillah,M. H., Rajoo, S., Martinez-Botas, R. F.: *Influence of speed and frequency towards the automotive turbocharger turbine performance under pulsating flow conditions*, Energy Convers. Manag., 80 (2014), pp. 416–428.

[13] Abidat, M., Hamidou, M. K., Hachemi, M., Hamel, M., Litim, S. A.: *Performance prediction of a mixed flow turbine*, Mécanique & Industries, 79 (2008), pp. 71–79.

[14] Čarija, Z., Marušić, E., Novak, Z., Fućak, S.: *Numerical analysis of aerodynamic characteristics of a bumped leading edge turbine blade*, Engineering Review, 34 (2014), 2, 93-101.

[15] Patankar, S. V., Spalding, D. B., Road, E.: *A calculation procedure for heat, mass and momentum transfer in parabolic flows*, Int. J. Heat Mass Transf., 1 (1972), pp. 1787–1806.

[16] Rhie, C. M., Chow, W.L.A.: *Numerical Study of the Turbulent Flow Past an Isolated Airfoil with Trailing Edge Separation*, AIAA J. 21 (1983), pp. 1525-1532.